Predicting electromagnetic counterparts using low-latency gravitational-wave data products

Cosmin Stachie,[1]⋆ Michael W. Coughlin,[2]⋆ Tim Dietrich,[3,4] Sarah Antier [ORCID],[5] Mattia Bulla,[6] Nelson Christensen,[1] Reed Essick,[7,8] Philippe Landry,[9] Benoit Mours,[10] Federico Schianchi[3] and Andrew Toivonen[2]

[1]*Artemis, Université Côte d'Azur, Observatoire Côte d'Azur, CNRS, CS 34229, F-06304 Nice Cedex 4, France*
[2]*School of Physics and Astronomy, University of Minnesota, Minneapolis, MN 55455, USA*
[3]*Institut für Physik und Astronomie, Universität Potsdam, Haus 28, Karl-Liebknecht-Str. 24/25, D-14476 Potsdam, Germany*
[4]*Max Planck Institute for Gravitational Physics (Albert Einstein Institute), Am Mühlenberg 1, Potsdam D-14476, Germany*
[5]*Université de Paris, CNRS, Astroparticule et Cosmologie, F-75013 Paris, France*
[6]*The Oskar Klein Centre, Department of Astronomy, Stockholm University, AlbaNova, SE-10691 Stockholm, Sweden*
[7]*Kavli Institute for Cosmological Physics, The University of Chicago, 5640 South Ellis Avenue, Chicago, IL 60637, USA*
[8]*Perimeter Institute for Theoretical Physics, 31 Caroline Street North, Waterloo, Ontario, N2L 2Y5, Canada*
[9]*Gravitational-Wave Physics & Astronomy Center, California State University, Fullerton, 800 N State College Blvd, Fullerton, CA 92831, USA*
[10]*Institut Pluridisciplinaire Hubert CURIEN, 23 Rue du Loess, BP28 F-67037 Strasbourg Cedex 2, France*

ABSTRACT

Searches for gravitational-wave counterparts have been going in earnest since GW170817 and the discovery of AT2017gfo. Since then, the lack of detection of other optical counterparts connected to binary neutron star or black hole–neutron star candidates has highlighted the need for a better discrimination criterion to support this effort. At the moment, low-latency gravitational-wave alerts contain preliminary information about binary properties and hence whether a detected binary might have an electromagnetic counterpart. The current alert method is a classifier that estimates the probability that there is a debris disc outside the black hole created during the merger as well as the probability of a signal being a binary neutron star, a black hole–neutron star, a binary black hole, or of terrestrial origin. In this work, we expand upon this approach to both predict the ejecta properties and provide contours of potential light curves for these events, in order to improve the follow-up observation strategy. The various sources of uncertainty are discussed, and we conclude that our ignorance about the ejecta composition and the insufficient constraint of the binary parameters by low-latency pipelines represent the main limitations. To validate the method, we test our approach on real events from the second and third Advanced Laser Interferometer Gravitational-Wave Observatory (LIGO)–Virgo observing runs.

Key words: gravitational waves – methods: statistical.

1 INTRODUCTION

The search for, detection, and characterization of the *kilonova* AT2017gfo (Coulter et al. 2017; Smartt et al. 2017; Abbott et al. 2017c), associated with the binary neutron star (BNS) merger GW170817 (Abbott et al. 2017a) and the short gamma-ray burst GRB170817A (Abbott et al. 2017d; Goldstein et al. 2017; Savchenko et al. 2017), has spurred on the search for more of these objects. These kilonovae are expected to be produced in many of the mergers of compact objects involving at least one neutron star (with another neutron star or black hole as companion). Powered by the neutron-rich outflows undergoing the radioactive decay of r-process elements (Lattimer & Schramm 1974; Li & Paczynski 1998; Metzger et al. 2010; Kasen et al. 2017), these ultraviolet/optical/infrared transients

produce emission approximately isotropically[1] and therefore are visible from nearly all directions. The properties of a kilonova, including the light curves and spectra, depend on the parameters of the original binary, including the masses (typically characterized by the chirp mass and mass ratio), spin angular momentum, and equation of state describing the neutron star interior (Bauswein, Baumgarte & Janka 2013a; Piran, Nakar & Rosswog 2013; Abbott et al. 2017a; Bauswein et al. 2017; Dietrich & Ujevic 2017; Radice et al. 2018b). The association between light curves and binary parameters has been used to place constraints on the character of the progenitor systems and quantity of matter expelled (e.g. Coughlin et al. 2017; Kasen et al. 2017; Perego et al. 2017; Smartt et al. 2017; Bulla 2019; Coughlin &

---

[1]We emphasize that, despite the approximately isotropic nature of the kilonovae, an angular dependence exists, as pointed out in e.g. Perego, Radice & Bernuzzi (2017), Kawaguchi, Shibata & Tanaka (2020) and Heinzel et al. (2021).

⋆ E-mail: scosmin@oca.eu (CS); michael.w.coughlin@gmail.com (MWC)

Dietrich 2019; Hinderer et al. 2019; Kawaguchi et al. 2020; Nicholl et al. 2021; Raaijmakers et al. 2021).

Searches for these counterparts are difficult for a variety of reasons, the most important one being the large sky localizations spanning ≈ 100–$10\,000\,\mathrm{deg}^2$ (Röver et al. 2007; Fairhurst 2009, 2011; Wen & Chen 2010; Grover et al. 2014; Sidery et al. 2014; Singer et al. 2014; Berry et al. 2015; Cornish & Littenberg 2015; Essick et al. 2015; Klimenko et al. 2016). Due to the size of the localizations, wide-field survey telescopes such as the Panoramic Survey Telescope and Rapid Response System (Pan-STARRS: Morgan et al. 2012), Asteroid Terrestrial-impact Last Alert System (ATLAS: Tonry et al. 2018), and Zwicky Transient Facility (ZTF: Bellm et al. 2018; Masci et al. 2018; Graham et al. 2019; Dekany et al. 2020), telescope networks such as the Gravitational-Wave Optical Transient Observer (GOTO-4: Gompertz et al. 2020) and Global Rapid Advanced Network Devoted to the Multi-messenger Addicts (GRANDMA (Antier et al. 2020a,b)), and future facilities such as BlackGEM (Bloemen et al. 2015) and the Vera C. Rubin Observatory's Legacy Survey of Space and Time (LSST: Ivezic et al. 2019) can cover extended regions most efficiently.

Given the limited telescope time, prioritization of gravitational-wave (GW) event candidates for follow-up is essential. This can include considerations such as the false-alarm rate of the event, the time of the merger (and therefore its relation to observability: Chen et al. 2017), and the properties of the merger itself. In particular, one quantity of interest is the apparent magnitude of the light curve in bands of a particular telescope during its observability window. This would limit observations to those objects that could feasibly be detected given the available telescope time and would help to prioritize between exposure time and sky coverage. An observation strategy, based on the idea of using low-latency GW products to predict electromagnetic (EM) properties, was first introduced in Salafia et al. (2017).

A number of previous studies tried to address the question of which compact binary merger should be the target of EM observations, e.g. Pannarale & Ohme (2014) were one of the first who used the remnant matter outside the final black hole as a proxy for the likelihood of potential EM counterparts. In addition, based on general-relativistic numerical simulations, empirical fitting formulas have also been derived for the ejected material and for the disc mass for BNS systems (Dietrich & Ujevic 2017; Coughlin et al. 2018a; Radice et al. 2018a; Dietrich et al. 2020; Nedora et al. 2020) and black hole–neutron star (BHNS) systems (Foucart 2012; Kawaguchi et al. 2016; Foucart, Hinderer & Nissanke 2018; Krüger & Foucart 2020).

Rapid analysis of the GW data in the era of advanced detectors is done by online low-latency pipelines. Traditionally there are two types of pipeline: one category targeting modelled signals and the other category tracking unmodelled events, both signals being general relativity predictions. Thereby pipelines of the first type search for well-modelled predicted signals (Dal Canton et al. 2014; Hooper et al. 2012; Aubin et al. 2020; Cannon et al. 2020), whereas the other type of pipeline searches for an excess of power in the data (Klimenko et al. 2008; Sutton et al. 2010; Lynch et al. 2017; Cornish et al. 2021). For the present study, we will use the templates released at the end of an analysis realized by the multi-band template analysis (MBTA) pipeline (Aubin et al. 2020), which searches for modelled binary mergers.

The real-time public data products (Abbott et al. 2018b) available to aid the EM/neutrino follow-up of binary merger candidates include 3D sky localization (Singer & Price 2016; Singer et al. 2016), the probability that the candidate is an astrophysical event (Kapadia et al. 2020), the probability of having at least one neutron star

– characterized by the probability of having one companion with mass below $3\,\mathrm{M}_\odot$ – and the probability of having remnant matter from the merger (Chatterjee et al. 2020), based on the disc mass prediction of Foucart et al. (2018). Overall, while extremely useful, this requires that all compact objects with masses below $3\,\mathrm{M}_\odot$ should be neutron stars, and there are some shortcomings to this analysis, e.g. not all BNS mergers will have a detectable EM counterpart (Bauswein et al. 2010; Coughlin et al. 2020b,c). A source classifier based on the template chirp mass was discussed equally in Dal Canton et al. (2020). Likewise, information from presumable compact binary coalescence EM precursors (Schnittman et al. 2018; Sridhar et al. 2021) might be envisaged in the future.

One issue to overcome, in addition to the statistical uncertainties, is the systematic errors in the low-latency template-based analysis. These searches use discrete template banks of waveforms to perform matched filtering on the data. For online searches, which are what we are concerned with here, the templates are characterized by masses m_1 and m_2 and the dimensionless aligned/anti-aligned spins of the binary elements along the orbital angular momentum of the binary, s_1 and s_2. These pipelines report the best-matching templates based on a detection statistic, giving a point estimate of these four quantities. The downside to this is clear: while quantities like the *chirp mass* m_{chirp} of systems are well measured, mass ratio and spin tend to be poorly constrained by this point estimate (Biscoveanu, Vitale & Haster 2019).

Additional, important supranuclear matter equation-of-state dependent information not provided by the low-latency pipelines includes estimates of the maximum mass, compactness, and/or tidal deformability of neutron stars. The maximum mass informs the classification of events as BNS, neutron star–black hole (NSBH), or binary black hole (BBH: Essick & Landry 2020).

The presence or absence of an EM counterpart to compact binary coalescence is determined by the amount of unbound baryonic material. The amount of ejecta, or even whether measurable ejecta exist, is directly linked to either the compactness of the neutron star(s) or their tidal deformability Λ in the combination

$$\tilde{\Lambda} = \frac{16}{13} \frac{(m_1 + 12m_2)m_1^4 \Lambda_1 + (m_2 + 12m_1)m_2^4 \Lambda_2}{(m_1 + m_2)^5}. \quad (1)$$

In general, the larger the tidal deformability, the less compact the stars and the higher the probability of gravitationally unbound material producing bright kilonovae.

In order to create a prior for the compactness C and maximum neutron-star mass, a choice of the neutron-star equation of state is necessary. The equations of state employed in this work is a zero-temperature relation between the pressure and the rest-mass energy density governing a fluid of baryons at supranuclear densities. Given an equation of state, there is a one-to-one correspondence between mass and tidal deformability, if the neutron star is completely made up of hadrons. Indeed, in the case of hybrid stars, hypothetical objects where deconfined quarks might exist (Alford, Han & Prakash 2013; Han et al. 2019; Lindblom 1998), the situation is different. Hybrid equations of state can support twin stars, neutron stars with the same mass but different central densities: the lower-density star's core is hadronic, while the higher-density star's is quark-like (Chatziioannou & Han 2020; Essick, Landry & Holz 2020a; Pang et al. 2020). For this study we consider only the case of hadron stars. Moreover, the supranuclear matter equation of state is important for the determination of a maximum neutron-star mass. Effectively, a soft (stiff) equation of state means more (less) compact neutron stars, corresponding to lower (higher) maximum mass. Unfortunately the supranuclear matter equation of state is not

Table 1. The MBTA preferred templates that maximize the signal-to-noise ratio for GW170817, GW190425, and GW190814. We include the name of the event, the mass of the more massive compact object m_1, the mass of the lighter compact object m_2, the chirp mass m_{chirp}, the mass ratio q, the projection of the heavier binary component's spin in the direction of the orbital angular momentum s_1, and the projection of the lighter binary component's spin in the direction of the orbital angular momentum s_2.

Event	m_1 ($\mathrm{M_\odot}$)	m_2 ($\mathrm{M_\odot}$)	m_{chirp} ($\mathrm{M_\odot}$)	q	s_1	s_2	χ_{eff}
GW170817	1.674	1.139	1.198	0.680	0.040	0.000	0.024
GW190425	2.269	1.305	1.487	0.575	0.080	-0.010	0.047
GW190814	36.881	2.093	6.522	0.057	0.340	0.960	0.373

known exactly, despite progress by different methods: simultaneous measurement of neutron-star mass and radius (e.g. Lattimer & Prakash 2001; Bogdanov et al. 2019; Miller et al. 2019; Riley et al. 2019; Raaijmakers et al. 2020); combination of gravitational tidal effects and EM data (e.g. Radice & Dai 2018; Dietrich et al. 2020; Landry, Essick & Chatziioannou 2020; Breschi et al. 2021); or a combination of nuclear physics and multi-messenger astronomy observations (e.g. Capano et al. 2020; Dietrich et al. 2020; Essick et al. 2020b).

As stated above, the mass ejecta constitute a key ingredient in the derivation of kilonova light curves. However, numerical simulations relying on general relativity are required to estimate this quantity. Despite the existence of such calculations (e.g. Goriely, Bauswein & Janka 2011; Tanaka & Hotokezaka 2013; Grossman et al. 2014; Rosswog et al. 2014; Bovard et al. 2017; Shibata et al. 2017; Dietrich et al. 2018; Radice et al. 2018a; Foucart et al. 2019), they are computationally expensive and cannot be performed directly in the minutes following a GW alert. For this reason, groups have proposed fits for the ejecta mass based on numerical-relativity simulations for both BNS mergers (e.g. Dietrich & Ujevic 2017; Coughlin et al. 2018a; Radice et al. 2018a; Dietrich et al. 2020; Nedora et al. 2020) and NSBH mergers (e.g. Foucart 2012; Kawaguchi et al. 2016; Foucart et al. 2018; Krüger & Foucart 2020). The present work aims to put together such existing tools, as well as parametrized kilonova light-curve models (Kasen et al. 2017; Bulla 2019), in order to predict EM counterparts based on only low-latency GW pipeline signal-to-noise distributions over the template bank.

The remainder of the article is structured as follows. In Section 2, we discuss the GW low-latency analysis and the current parameters released to aid observers. Section 3 presents how we convert component binary parameters to mass ejecta and we discuss the two models that we employ in the computation of kilonova light curves in Section 4. We validate our method on GW events from recent LIGO–Virgo observing runs in Section 5. We summarize the performance of this tool and suggest improvements for future work in Section 6.

2 ADDRESSING THE POINT ESTIMATE UNCERTAINTIES

MBTA (Aubin et al. 2020) is a modelled search pipeline based on matched filtering, which compares the inspiral waveforms from a "bank" of templates with the data. Templates are distributed across the parameter space such that any point has a good match with at least one of the templates of the bank, the minimal match value typically being 97 per cent (for GW170817, here we used 99 per cent). The template bank is therefore a rather uniform sampling of the parameter space. This template bank is applied separately to each detector;

coincident triggers are those that share the same template parameters and have time delays consistent with astrophysical sources.

MBTA splits this analysis into two or more frequency bands, i.e. instead of comparing all the frequency components of the data with those of the template, the frequency bands of the detector data and templates are split into multiple bands.[2] The matched filter is computed within each band, and the signal-to-noise ratios corresponding to the different bands are combined to assign an overall statistical significance to the template. This procedure reduces the computational cost, such that the pipeline is able to analyse the LIGO–Virgo data with a subminute latency using modest computing resources (about 150 cores). It is worth mentioning that the analysis pursued in this work should apply equally well to all low-latency pipelines.

2.1 Template uncertainties

As mentioned previously, during observing runs O2 and O3, the low-latency alerts released by the LIGO Scientific Collaboration and Virgo Collaboration (LVC) consisted of the binary parameters of the template with the highest statistical significance. In Table 1, these parameters are displayed for GW170817, GW190425, and GW190814. The reason we focus on these events is that they are unambiguously confirmed binary systems that have a non-negligible probability of possessing at least one neutron star. However, for the present work, we consider not only the 'best' template, with corresponding $\mathrm{SNR_{max}}$, but all templates with signal-to-noise ratio $\mathrm{SNR} > \mathrm{SNR_{max}} - 3$, where $\mathrm{SNR_{max}}$ is the signal-to-noise ratio of the 'best' template. The motivation for this choice is the desire to realize rapid parameter estimation based on these neighbourhood templates, which are within three standard deviations of the best template and therefore capture 99.7 per cent of the parameter information.

2.2 Using multiple templates

For one event, MBTA provides the list of templates that have been triggered, with their SNR. For each of them, a weight, w, is given to capture the probability that this template is the most likely to describe the event. It is based on the SNR of the template i relative to the maximum SNR: $\mathrm{dSNR} = \mathrm{SNR_{max}} - \mathrm{SNR}_i$, i.e. the number of standard deviations for this template compared with the best template. The weights are computed by sorting the templates by increasing dSNR, and then obtaining the difference of the error function with the following template: $w_i = \mathrm{erf}(\mathrm{dSNR}_{i+1}/\sqrt{2}) - \mathrm{erf}(\mathrm{dSNR}_i/\sqrt{2})$. Before being used, the weights are smoothed by

---

[2]Other pipelines also perform multi-band analyses, an example being Sachdev et al. (2019).

Table 2. The median, upper limits (90th percentile), and lower limits (10th percentile) for GW170817, GW190425, and GW190814 parameters for the chirp mass m_{chirp}, the mass ratio q, and the effective spin χ_{eff}. These quantities are obtained from the set of templates generated as explained in Section 2.2. The same quantities obtained from offline PE posteriors are also illustrated for comparison. A missing m_{chirp} upper/lower limit means that the deviation from the median value is less than $0.001\,\mathrm{M_{\odot}}$. The PE samples have been introduced previously (Abbott et al. 2019, 2020b).

Event	MBTA			PE		
	m_{chirp} $(\mathrm{M_{\odot}})$	q	χ_{eff}	m_{chirp} $(\mathrm{M_{\odot}})$	q	χ_{eff}
GW170817	$1.198_{-0.001}$	$0.756^{+0.068}_{-0.157}$	$0.029^{+0.017}_{-0.018}$	1.186	$0.864^{+0.107}_{-0.12}$	$0.003^{+0.01}_{-0.007}$
GW190425	$1.487^{+0.001}_{-0.002}$	$0.784^{+0.121}_{-0.229}$	$0.026^{+0.024}_{-0.056}$	$1.437^{+0.018}_{-0.016}$	$0.657^{+0.266}_{-0.21}$	$0.058^{+0.079}_{-0.041}$
GW190814	$6.474^{+0.125}_{-0.134}$	$0.058^{+0.178}_{-0.008}$	$0.321^{+0.094}_{-0.817}$	$6.09^{+0.046}_{-0.043}$	$0.111^{+0.006}_{-0.007}$	$-0.003^{+0.047}_{-0.045}$

averaging them with their two adjacent templates in dSNR. With this procedure, the sum of all weights is one. We will use the weights as the 'significance' measure for a given template.

The input data are represented by a list of templates, which is a 5-tuple (m_1, m_2, s_1, s_2, w), where m_1, m_2 $(m_1 \geq m_2)$ are the masses of the binary components, s_1, s_2 are the projections of the spins on to the direction of the orbital angular momentum, and w is the normalized weight. In Table 2, we list the median, lower, and upper limits for the binary parameters obtained by this procedure. The corresponding values obtained by the more expensive offline parameter estimation method (Veitch et al. 2015, hereafter PE) are also presented. One can observe that there is very good similarity (at most a few per cent deviation) between PE and our method for m_{chirp}. On the other hand, the mass ratio and effective spin distributions can be very different (more than 100 per cent in the case of GW190814). One could imagine different ways to address the problem of these latter distributions. A possibility might be to consider a population prior based on the already detected binary compact merger events as suggested in e.g. Essick & Landry (2020), Fishbach, Essick & Holz (2020b), Fishbach, Farr & Holz (2020a), Mandel (2010), and Abbott et al. (2020a); however, this procedure might introduce additional biases if as yet unobserved populations of compact binaries exist.

In the following, the intrinsic masses and spins estimated here will be used for the computation of the mass and velocity of ejecta in Section 3. It is worth mentioning that over the past years several rapid parameter estimation efforts have been realized (e.g. Pankow et al. 2015; Lange, O'Shaughnessy & Rizzo 2018; Smith et al. 2020).

3 DYNAMICAL AND DISC WIND EJECTA FROM TEMPLATES

Two important features of a kilonova light curve are the overall luminosity and the relative colours in the photometric bands. The former is related to the amount of matter as well as the object's distance, while the latter is related to its composition, such as the lanthanide fraction, and the viewing angle to the binary. The mass of the unbound material ejected from the system is a key parameter for the computation of kilonova light curves. The ejecta mass and further ejecta properties depend on both the nature of the binary – BNS, NSBH, or BBH – and the supranuclear equation of state describing the neutron-star material.

3.1 Equation of state of a neutron star

Low latency/near real-time GW searches do not provide information concerning the compactness of the compact objects. However, for a fixed equation of state that does not support twin stars, fixing

the mass of a neutron star fixes the baryonic mass m^{bar}. Equally, it fixes the radius R and also the compactness by means of the relation $C = Gm/(Rc^2)$, where G, m, and c are the gravitational constant, the mass of the compact object, and the speed of light in a vacuum. In the literature, there are several equation-of-state candidates. One possibility is to assume a popular one (e.g. Douchin & Haensel 2001), another to sample a number of equations of state simultaneously (e.g. Landry & Essick 2019; Capano et al. 2020; Dietrich et al. 2020). We do the latter using the four-parameter spectral representation of the equation of state presented in Abbott et al. (2018a). More specifically, the spectral representation decomposes the equation of state's adiabatic index Γ into a polynomial in the logarithm of the pressure with coefficients $\{\gamma\} = (\gamma_0, \gamma_1, \gamma_2, \gamma_3)$ (Lindblom 2010; Lindblom & Indik 2012; Lindblom & Indik 2014). Given the specification of a low-density crust model, which we take to be *Skyrme Lyon* (SLY) (Douchin & Haensel 2001), and the requirement of smooth matching, the equation of state is uniquely specified by its spectral parameters.

For every (m_1, m_2), we sample the compactness independently for each component. To do so, we marginalize over the 2396 GW170817-like equations of state presented in Abbott et al. (2018a). For each equation of state, the compactnesses $C_1 = C(m_1)$ and $C_2 = C(m_2)$, as well as the baryonic mass of the lighter object $m_2^{\mathrm{bar}} = m^{\mathrm{bar}}(m_2)$, are calculated, and a maximum neutron-star mass is prescribed. For each sample, if one of the components has a mass higher than this threshold (defined by the equation-of-state dependent maximum neutron-star mass), it is considered to be a black hole.[3] This allows us to put each sample in one of three categories: BNS, NSBH, and BBH. This marginalization procedure yields a list of 7-tuples $(q, m_{\mathrm{chirp}}, \chi_{\mathrm{eff}}, C_1, C_2, m_2^{\mathrm{bar}}, f)$, where $f \in \{0, 1, 2\}$ stands for the type of binary: BNS ($f = 0$) or NSBH ($f = 1$) or BBH ($f = 2$). The size of this list of samples is equal to the number of initial MBTA templates times 2396 (the number of equations of state). For those samples consistent with BBHs, we assume that there are no ejecta. For the BNS and NSBH cases, we calculate the ejecta mass and velocity as described in the following.

3.2 Ejecta parameters: BNS

In general, there are (at least) two ejecta mass components contributing to the kilonova: the dynamical ejecta and the disc mass. We follow Dietrich et al. (2020) and use the formula $m_{\mathrm{ej}} = M_{\mathrm{ej}}^{\mathrm{dyn}} + \zeta M_{\mathrm{disc}}$ to

---

[3]Note that spinning NSs can support ~ 20 per cent more mass (Breu & Rezzolla 2016), but we neglect this, as all known Galactic NSs have relatively low spins.
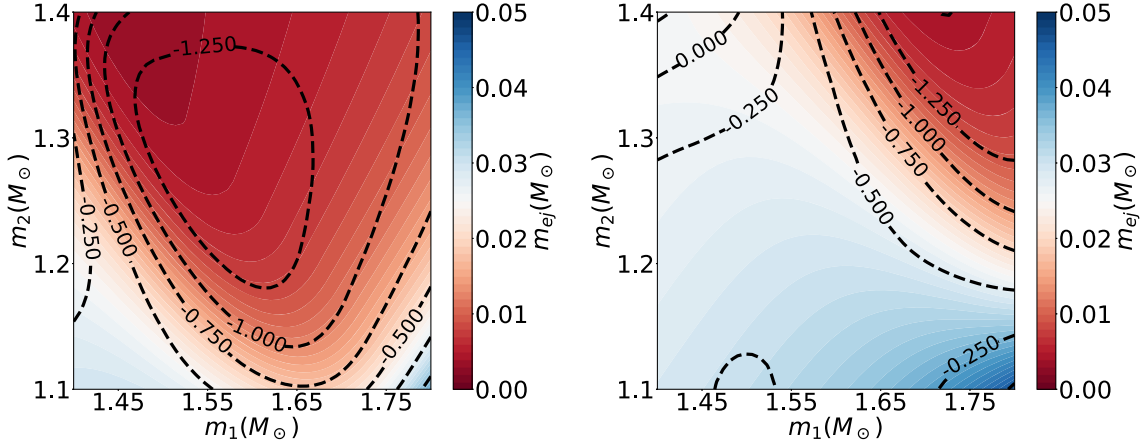
Figure 1. In colour, we show the predicted mass ejecta obtained by our model for BNS mergers with different binary component masses. The level lines show the relative difference that exists between our model and the one from Nedora et al. (2020). The quantity illustrated by those lines is $2(m_{\mathrm{ej}} - m_{\mathrm{ej}}^{\mathrm{NEA}})/(m_{\mathrm{ej}} + m_{\mathrm{ej}}^{\mathrm{NEA}})$, where $m_{\mathrm{ej}}^{\mathrm{NEA}}$ is the predicted mass ejecta computed by the model in Nedora et al. (2020). The left (respectively right) panel corresponds to a fixed spectral equation of state with parameters $\{\gamma\} = (0.5485, 0.3767, -0.0690, 0.0035)$ (respectively $\{\gamma\} = (1.4777, -0.3225, 0.0694, -0.0046)$); this equation of state predicts a radius of 11.3 km (13.0 km) and a tidal deformability of 232 (663) for a 1.4-$M_{\odot}$ neutron star, as well as a maximum Tolman–Oppenheimer–Volkov mass of 2.00 $M_{\odot}$ (2.43 $M_{\odot}$).

represent the ejecta proportions. Here, $M_{\mathrm{ej}}^{\mathrm{dyn}}$ stands for the mass of the dynamical ejecta, and M_{disc} stands for the disc mass. From the disc, a fraction of matter (ζ) will become unbound through disc winds caused by several physical phenomena, e.g. neutrino radiation, magnetic-driven winds, or the redistribution of angular momentum. We assume, based on numerical-relativity simulations, that $\zeta = 0.15$ of the entire disc mass gets gravitationally unbound and ejected from the system (e.g. Fernández et al. 2015, 2019; Siegel & Metzger 2018; Christie et al. 2019).

To estimate the dynamical ejecta, we use the fitting formula from Coughlin et al. (2019a):

$$\log_{10} M_{\mathrm{ej}}^{\mathrm{dyn}}(\mathrm{M}_{\odot}) = \left[a \frac{(1 - 2C_1)m_1}{C_1} + b\, m_2 \left(\frac{m_1}{m_2} \right)^n + \frac{d}{2} \right] \\ + [1 \leftrightarrow 2],$$

where m_1 and C_1 (respectively m_2 and C_2) are the mass and compactness of the heavier (respectively lighter) binary component, and $a = -0.0719$, $b = 0.2116$, $d = -2.42$, $n = -2.905$ are fitting coefficients. To estimate the disc mass, we use the fitting formula from Dietrich et al. (2020):

$$\log_{10} M_{\mathrm{disc}}(\mathrm{M}_{\odot}) \\ = \max \left\{ -3, a \left[1 + b \tanh \left(\frac{c - (m_1 + m_2)/M_{\mathrm{thresh}}}{d} \right) \right] \right\},$$

where the floor value of 10^{-3} $\mathrm{M}_{\odot}$ is added, as it is difficult to resolve smaller masses in numerical relativity (see e.g. Dietrich & Ujevic 2017; Radice et al. 2018a). Here, M_{thresh} is the minimum total mass such that prompt collapse occurs after coalescence of two neutron stars; this expression is calculated as in Bauswein, Baumgarte & Janka (2013b). While the parameters $c = 0.953$ and $d = 0.0417$ are fixed, the parameters a and b are not constant but mass-ratio dependent; cf. Dietrich et al. (2020) for a detailed discussion.

For comparison, in Nedora et al. (2020), the disc and dynamical masses are calculated by means of a formula using the mass ratio and the tidal deformability $\tilde{\Lambda}$. An illustration of the ejecta dependence on the binary component masses, as well as a comparison with the predictions of this latter model, is presented in Fig. 1.

This demonstrates broad qualitative consistency, but differences of ~100 per cent between different predictions are common. This is mainly due to the different sets of numerical-relativity simulations used for the calibration and different functional forms for the phenomenological fits. In addition, one has to point out that, while the numerical-relativity simulations provide a description of the merger and postmerger dynamics and are capable of predicting (to some extent) the amount of ejecta, the individual predictions are usually connected with large uncertainties due to, among other things, (i) the absence of accurate microphysical modelling of the fluid as well as the inclusion of magnetic fields, (ii) complications during the simulation of relativistic fluids, when shocks and discontinuities form, (iii) inaccuracies during simulation of expanding and decompressing ejected material, and (iv) a limited set of numerical simulations that do not cover the entire BNS parameter space. Nonetheless, some relations between the binary parameters and the amount of ejecta are noticeable and we find that lower compactness and/or smaller individual masses in general produce more ejecta.

We also compute the velocity of the ejecta. Following Coughlin et al. (2019a), we use $v_{\mathrm{ej}} = [a(1 + c\, C_1 \frac{m_1}{m_2} + \frac{b}{2})] + [1 \leftrightarrow 2]$, where the fit coefficients are $a = -0.3090$, $b = 0.657$, and $c = -1.879$. The result in this formula is expressed in units of the speed of light.

3.3 Ejecta parameters: NSBH

Similarly to the BNS merger case, we assume that NSBH ejecta have (at least) two components: dynamical ejecta and disc wind ejecta. In a NSBH system, the only baryonic matter responsible for any EM signature is that contained in the neutron star, i.e. m_2^{bar}. As in the BNS case, we assume that 15 per cent of the disc mass becomes gravitationally unbound over time, where the disc mass is estimated according to Foucart et al. (2018) as

$$M_{\mathrm{disc}}(\mathrm{M}_{\odot}) = m_2^{\mathrm{bar}} \max \left(0, \alpha \frac{1 - 2C_2}{\eta^{1/3}} - \beta r_{\mathrm{ISCO}} \frac{C_2}{\eta} + \gamma \right)^{\delta},$$

with m_2^{bar}, C_2, $\eta = \frac{m_1 m_2}{m_1 + m_2}$, and r_{ISCO} being the baryonic mass of the neutron star, the compactness of the neutron star, the reduced mass,
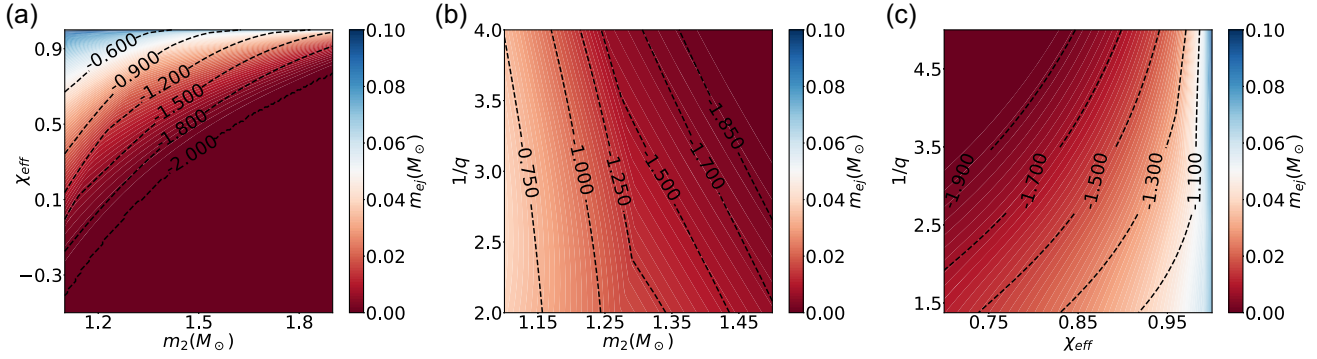
Figure 2. Amount of ejected mass (on the coloured axis) for NSBH mergers with different binary characteristics: (a) $\chi_{\rm eff}$ versus m_2, keeping $1/q = m_1/m_2 = 2$; (b) inverse mass ratio $1/q$ versus neutron-star mass m_2, keeping $\chi_{\rm eff} = 0.6$; and (c) $1/q$ versus $\chi_{\rm eff}$ at constant $m_2 = 1.6\,{\rm M_\odot}$. The level lines show the relative difference in dynamical ejecta that exists between our model and the one proposed in Kawaguchi et al. (2016). More precisely, the values of the level lines indicate the quantity $2(M^{\rm dyn} - M^{\rm dyn}_{\rm KAW})/(M^{\rm dyn} + M^{\rm dyn}_{\rm KAW})$, where $M^{\rm dyn}_{\rm KAW}$ is the dynamical ejecta predicted by Kawaguchi et al. (2016). These simulations use the equation of state with parameters $\{\gamma\} = (0.3268, 0.4456, -0.0586, 0.0016)$, which predicts a radius of 12.4 km and a tidal deformability of 458 for a 1.4-$\rm M_\odot$ neutron star, the maximum Tolman–Oppenheimer–Volkov mass being 2.37 $\rm M_\odot$.

and the innermost stable circular orbit. The coefficients are $\alpha = 0.4064$, $\beta = 0.1388$, $\gamma = 0.2551$, and $\delta = 1.7612$. The mass of the dynamical ejecta is calculated from Krüger & Foucart (2020):

$$M^{\rm dyn}({\rm M_\odot}) = m_2^{\rm bar}\left[a_1\left(\frac{m_1}{m_2}\right)^{n_1}\frac{1 - 2C_2}{C_2} - a_2\left(\frac{m_1}{m_2}\right)^{n_2}\frac{r_{\rm ISCO}}{m_1} + a_4\right].$$

In this formula, m_1 is the mass of the black hole and the fitting coefficients are $a_1 = 0.007116$, $a_2 = 0.001436$, $a_4 = -0.02762$, $n_1 = 0.8636$, and $n_2 = 1.6840$.

The dependence of ejected mass on various parameters is illustrated in Fig. 2. One can easily observe that the higher the effective spin, the higher the mass ejecta. At very high inverse mass ratios, for a constant m_2, the neutron star is swallowed by the black hole before being disrupted; cf. Shibata & Taniguchi (2011), Foucart (2020), and references therein for a detailed description. Kawaguchi et al. (2016) propose similar ejecta fits for the dynamical ejecta. A comparison between those predicted dynamical ejecta and our choice of $M^{\rm dyn}$ is equally proposed in Fig. 2.

We also compute the velocity of the ejecta. Following Kawaguchi et al. (2016): $v_{\rm ej} = \alpha(m_1/m_2) + \beta$ with $\alpha = 0.01533$ and $\beta = 0.1907$. The result in this formula is expressed in units of the speed of light.
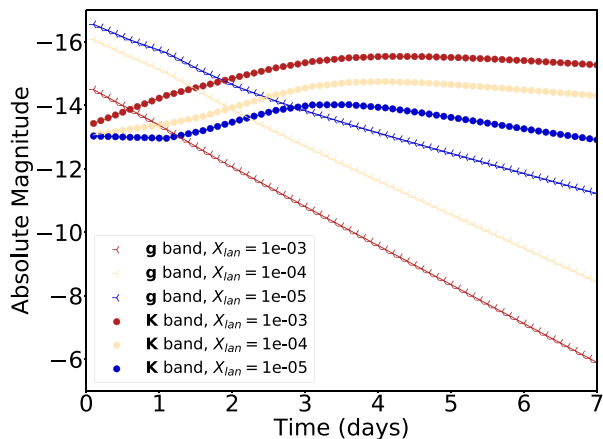
4 LIGHT CURVES

Once the calculations presented in the previous section are performed, we have 2396 times $n_{\rm templates}$ $(m_{\rm ej}, v_{\rm ej})$ tuples, where $n_{\rm templates}$ stands for the number of MBTA templates. This set is downsampled to a set of size 1000 for computational cost reasons. The value of 1000 is justified by the similarity between the $m_{\rm ej}$ distributions of the initial and downsampled sets. Such a size of the downsampled set allows an overlap of higher than 80 per cent between the initial and new mass ejecta distributions in the case of GW170817 and GW190425. We now use light-curve models to translate the ejecta properties into observed light curves. We use the light-curve models proposed in Kasen et al. (2017) (hereafter *Model I*) and Bulla (2019) (hereafter *Model II*). These are radiative transfer simulations predicting light curves and spectra, based on the wavelength-dependent emissivity and opacity taking place at the atomic scale. In particular, we use the surrogate technique first presented in Coughlin et al. (2018b) to

create a grid of light curves in the photometric bands u, g, r, i, z, y, J, H, and K for a set of model parameters. Using Gaussian process regression, one can predict the light curve for any input parameters. A common parameter for the two models is the total ejecta mass, i.e. the sum of the dynamical and wind ejecta. That is equivalent to saying that we use the one-component ejecta model presented in Coughlin et al. (2018b), i.e. the EM signal luminosity is calculated at once for the entire ejected matter. This is in contrast to the case of the two-component model, where the brightnesses due to disc winds and dynamical ejecta are calculated separately and added up a posteriori. Therefore the statistical errors regarding the two-component model are already large enough that this choice does not make a difference; cf. e.g. Kawaguchi et al. (2020) and Heinzel et al. (2021) for a discussion about uncertainties and viewing-angle dependences of the kilonova signal. In addition, for *Model II* we use the grid first presented in Coughlin et al. (2020a), but extended for better coverage of the lower- and upper-mass end (it goes from $10^{-6}\,{\rm M_\odot}$ to 1 $\rm M_\odot$). This upgrade will be made publicly available.[4] It is noteworthy to mention that, for all the light-curve contours presented in this section, two extra magnitude errors have been added, i.e. the upper (lower) magnitude limits have been raised (lowered) by 1, in order to be robust against twice the errors in thermalization rate and/or ejecta geometry.

4.1 *Model I* light-curve model

Model I presented in Kasen et al. (2017) solves the relativistic radiation transport Boltzmann equation governing the interior of a radioactive plasma. In this way, both the thermal and spectral-line radiation determine the final wavelength-dependent luminosity and time-scale of the light curve. The *Model I* light curve is a function of $m_{\rm ej}$, $v_{\rm ej}$, and $X_{\rm lan}$, where $m_{\rm ej}$ is the ejected mass, $v_{\rm ej}$ is the velocity of the ejecta, and $X_{\rm lan}$ is the lanthanide fraction. The effects of the first two parameters are simple and intuitive: the higher the amount of ejecta, the brighter and longer-lasting the electromagnetic signal; meanwhile, the higher the speed of the ejecta, the brighter and shorter (the ejecta is expanding faster) the kilonova. The latter parameter $X_{\rm lan}$ expresses the composition of the ejecta and controls the opacity at the atomic scale. Therefore, for ejecta containing heavier elements,

---

[4]https://github.com/mbulla/kilonova_models

Figure 3. Absolute magnitude versus time for kilonovae with different lanthanide percentages X_{lan}, as predicted by *Model I*. For all the light curves, the values of mass and velocity of the ejecta are set to $m_{ej} = 0.05\,M_\odot$ and $v_{ej} = 0.15c$. The plot corresponds to the '*g*' and '*K*' photometric bands. The *x*-axis origin corresponds to the merger time.

the density of spectral lines is larger. This aspect will imply a higher opacity and, with that, a fading of the brightness on larger time-scales.

We compute m_{ej} and v_{ej} as described in Section 3; X_{lan}, on the other hand, requires further assumptions. In general, a larger X_{lan} yields redder light curves. In Fig. 3, there is an example of the dependence of the light curve on the lanthanide fraction. One can observe that an uncertainty in X_{lan} of three orders of magnitude leads to an uncertainty in the '*g*' band of more than 2 (respectively 5) magnitudes at the end of the first (seventh) day.

4.2 *Model II* light-curve model

Model II (Bulla 2019; Coughlin et al. 2020a) is also based on Monte Carlo radiative transfer simulations. Unlike *Model I*, which is 1D and has geometry-independent parameters, *Model II* is 2D, i.e. axisymmetric, and the ejecta are considered to have two components with different compositions and locations determined with respect to the geometry of the binary. Therefore, the EM signal depends on the position of the external observer, i.e. the viewing angle. In this model, one component is lanthanide-rich and is situated around the plane of the merger, whereas a second component is lanthanide-free and positioned at higher latitudes. The interplay between the two components is captured by the half-opening angle of the lanthanide-rich component, Φ, while the position of the observer is controlled by the viewing angle θ_{inc}.

The two models differ in their considerations of ejecta opacities. While in *Model I* the lanthanide fraction can take any value and the opacities are calculated correspondingly, in *Model II* the composition of the two ejecta components is fixed and for simplicity we assume just two different compositions and corresponding opacities (one for each component, see Bulla 2019).

Model II depends on the following parameters: m_{ej}, θ_{inc}, and Φ, where m_{ej} is as above the total mass of the ejecta. Because MBTA samples do not provide θ_{inc} for O2 and O3, and there is no imprint of Φ in the GW signal, some additional assumptions are necessary. For illustration purposes, Fig. 4 shows the dependence of the EM light curves for different prior choices, where an increase in the opening angle reddens the light curve, whereas an increase in the inclination angle will lower the luminosity and redden the signal.
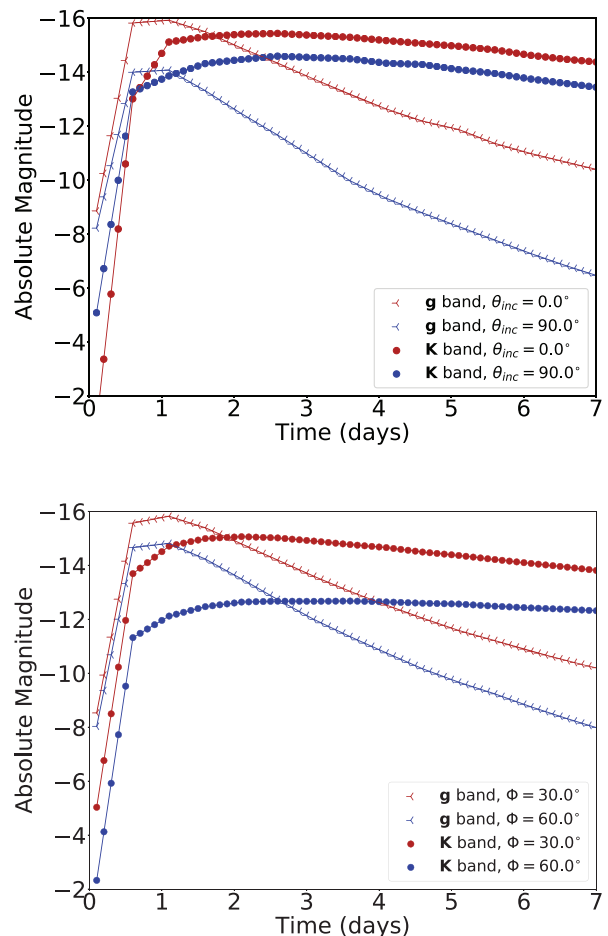
Figure 4. Absolute magnitude versus time for kilonovae with different inclination angles θ_{inc} (top) and opening angles Φ (bottom) as expected in '*g*' and '*K*' photometric passbands and as predicted by *Model II*. For the top plot, we set $m_{ej} = 0.05\,M_\odot$ and $\Phi = 45°$, while for the bottom plot we set $m_{ej} = 0.05\,M_\odot$ and $\theta_{inc} = 45°$. On both sides, the *x*-axis origin corresponds to the merger time.

4.3 Sources of uncertainty

Our predicted light curves have assigned uncertainties. These are due to either inaccurate measurement of the GW strain by GW interferometers or our limited knowledge about the composition of the stars and the way matter behaves at supranuclear densities. More specifically, there are the following sources of uncertainty: the inaccurate measurement of binary parameters such as the chirp mass, the mass ratio, and the dimensionless effective spin; the uncertainty induced by the GW170817-like equation-of-state marginalization; the errors produced by the mass (as well as the velocity) ejecta fits; and finally missing knowledge of the ejecta chemical composition, which in the case of *Model I* (respectively *Model II*) is represented by the lanthanide fraction (respectively the half-opening angle of the lanthanide-rich ejecta component). In this section we illustrate the impact of these uncertainty sources on the light curves and on '*HasEjecta*', defined as the probability of having $m_{ej} > 3 \times 10^{-4}\,M_\odot$. The value of this threshold is argued by the fact that $1.5 \times 10^{-4}\,M_\odot$ is the minimum mass ejecta for a BNS (based on the disc wind mass fit), and as a consequence we consider that a configuration produces noticeable ejecta when the total ejecta is at least twice as large as this default value. We start with a binary

Table 3. *HasEjecta* and absolute magnitude, assigned with upper (10th percentile) and lower (90th percentile) limits, for different binaries and different sources of uncertainty. The real parameters, m_1^{fixed}, m_2^{fixed}, $\chi_{\text{eff}}^{\text{fixed}}$, of the binaries are provided in the first three columns. When there is no marginalization over the entire set of 2396 equations of state, EOS$^{\text{fixed}}$ always corresponds to $\{\gamma\} = (1.4777, -0.3225, 0.0694, -0.0046)$ and associates to a 1.4-M$_\odot$ neutron star, a radius of 13.0 km and a tidal deformability of 663, while the maximum Tolman–Oppenheimer–Volkov mass is 2.43 M$_\odot$. The fourth column indicates either the unique source of uncertainty (MBTA; equation of state; m_{ej}, v_{ej}; X_{lan}), whether no uncertainty was considered, or whether all the combined uncertainty sources have been taken into account. The absolute magnitudes and their error bars are reported for the g and K photometric filters after the first, second, and third day, with respect to the coalescence time. All the simulations have been realized with *Model I*.

| | Binary | | | | Absolute magnitude | | | | | |
| | | | | | 1 day | | 2 days | | 3 days | |
m_1^{fixed} (M$_\odot$)	m_2^{fixed} (M$_\odot$)	$\chi_{\text{eff}}^{\text{fixed}}$	Source of uncertainty	*HasEjecta* (%)	g band	K band	g band	K band	g band	K band
			no uncertainty		-13.5	-12.7	-11.9	-13.0	-10.3	-12.6
			MBTA	100	$-13.7^{-1.9}_{+0.5}$	$-12.9^{-1.1}_{+0.4}$	$-12.2^{-2.3}_{+0.7}$	$-13.4^{-1.1}_{+0.7}$	$-10.7^{-2.8}_{+0.8}$	$-13.1^{-1.9}_{+1.0}$
1.6	1.4	0.01	equation of state	100	$-11.9^{-1.6}_{+0.3}$	$-12.1^{-0.6}_{+0.2}$	$-10.0^{-1.9}_{+0.6}$	$-11.6^{-1.5}_{+0.3}$	$-8.2^{-2.2}_{+0.8}$	$-11.2^{-1.4}_{+0.2}$
			m_{ej}, v_{ej}		$-13.5^{-0.5}_{+1.5}$	$-12.9^{-0.8}_{+1.2}$	$-11.8^{-1.0}_{+2.3}$	$-12.8^{-1.0}_{+0.6}$	$-10.3^{-1.7}_{+3.1}$	$-12.1^{-0.8}_{+0.3}$
			X_{lan}		$-14.0^{-0.3}_{+4.8}$	$-12.3^{-2.2}_{+0.3}$	$-13.0^{-0.6}_{+4.9}$	$-12.2^{-2.7}_{+0.9}$	$-12.2^{-1.0}_{+4.9}$	$-11.3^{-3.4}_{+2.2}$
			all	100	$-12.9^{-2.8}_{+4.1}$	$-13.0^{-1.7}_{+2.4}$	$-11.9^{-3.0}_{+4.7}$	$-12.9^{-2.7}_{+4.7}$	$-11.1^{-3.3}_{+4.6}$	$-12.3^{-2.8}_{+6.8}$
			no uncertainty		-13.7	-13.0	-12.1	-13.2	-10.5	-12.7
			MBTA	100	$-13.7^{-1.8}_{+2.2}$	$-12.9^{-0.8}_{+1.1}$	$-12.1^{-2.2}_{+2.7}$	$-13.3^{-1.2}_{+2.1}$	$-10.6^{-2.8}_{+3.2}$	$-13.0^{-2.1}_{+2.1}$
2.0	1.4	0.10	equation of state	96	$-13.8^{-0.3}_{+2.9}$	$-13.1^{-0.3}_{+1.8}$	$-12.2^{-0.6}_{+3.0}$	$-13.5^{-0.4}_{+2.5}$	$-10.7^{-0.8}_{+2.6}$	$-13.0^{-0.3}_{+2.5}$
			m_{ej}, v_{ej}		$-13.6^{-0.3}_{+1.4}$	$-13.2^{-0.6}_{+1.3}$	$-12.1^{-0.7}_{+2.1}$	$-13.0^{-0.7}_{+0.6}$	$-10.7^{-1.4}_{+2.9}$	$-12.3^{-0.7}_{+0.3}$
			X_{lan}		$-14.2^{-0.3}_{+4.6}$	$-12.6^{-2.2}_{+0.3}$	$-13.2^{-0.6}_{+4.6}$	$-12.3^{-2.8}_{+1.0}$	$-12.4^{-1.0}_{+4.5}$	$-11.5^{-3.4}_{+2.3}$
			all	98	$-12.7^{-2.7}_{+4.0}$	$-12.8^{-1.7}_{+2.3}$	$-11.6^{-3.0}_{+4.1}$	$-12.6^{-2.3}_{+4.6}$	$-10.7^{-3.3}_{+4.3}$	$-11.8^{-3.1}_{+6.5}$
			no uncertainty		-11.5	-11.8	-9.2	-11.4	-6.9	-11.0
			MBTA	53	$-10.3^{-4.4}$	$-11.2^{-2.3}$	$-9.2^{-4.1}_{+0.1}$	$-10.3^{-3.9}$	$-8.1^{-4.0}_{+1.3}$	$-9.0^{-5.1}$
4.0	1.4	0.10	equation of state	40	$-10.3^{-1.0}$	$-11.2^{-0.4}_{+0.1}$	$-9.2_{+1.2}$	$-10.3^{-0.8}$	$-8.1_{+2.8}$	$-8.9^{-1.8}$
			m_{ej}, v_{ej}		$-11.6^{-1.1}_{+1.2}$	$-11.9^{-0.9}_{+0.6}$	$-9.7^{-1.6}_{+2.0}$	$-11.2^{-0.7}_{+0.3}$	$-7.9^{-2.3}_{+3.1}$	$-10.7^{-0.2}_{+0.2}$
			X_{lan}		$-12.2^{-0.5}_{+4.8}$	$-11.0^{-2.7}_{+0.6}$	$-11.0^{-1.1}_{+4.9}$	$-9.8^{-3.7}_{+2.8}$	$-9.8^{-1.8}_{+5.9}$	$-9.1^{-3.7}_{+5.9}$
			all	27	$-10.4^{-2.5}_{+0.1}$	$-11.2^{-1.7}$	$-9.3^{-2.5}_{+0.1}$	$-10.3^{-2.5}_{+0.1}$	$-8.2^{-2.8}_{+0.1}$	$-8.9^{-3.0}_{+0.1}$
			no uncertainty		-15.6	-13.7	-14.4	-14.6	-13.4	-15.2
			MBTA	54	$-10.7^{-5.2}_{+0.3}$	$-11.2^{-3.0}$	$-9.2^{-5.5}$	$-10.5^{-4.3}_{+0.2}$	$-8.1^{-5.8}$	$-10.1^{-4.9}_{+1.2}$
4.0	1.4	0.70	equation of state	100	$-14.9^{-0.7}_{+1.2}$	$-13.5^{-0.3}_{+0.6}$	$-13.5^{-0.8}_{+0.7}$	$-14.2^{-0.5}_{+1.7}$	$-12.3^{-1.1}_{+1.7}$	$-14.3^{-0.9}_{+1.1}$
			m_{ej}, v_{ej}		$-15.1^{-0.5}_{+0.7}$	$-13.8^{-0.6}_{+1.0}$	$-13.9^{-0.5}_{+1.2}$	$-14.6^{-0.3}_{+1.0}$	$-13.3^{-0.4}_{+1.9}$	$-14.3^{-1.1}_{+0.3}$
			X_{lan}		$-16.1^{-0.1}_{+5.3}$	$-13.3^{-1.9}_{+0.1}$	$-15.0^{-0.4}_{+5.0}$	$-14.2^{-1.7}_{+0.2}$	$-14.4^{-0.6}_{+5.0}$	$-14.3^{-1.9}_{+0.6}$
			all	44	$-10.4^{-5.2}_{+0.2}$	$-11.2^{-3.2}_{+0.1}$	$-9.3^{-5.5}_{+0.2}$	$-10.3^{-4.5}_{+0.1}$	$-8.3^{-6.0}_{+0.2}$	$-9.0^{-5.8}_{+0.2}$
			no uncertainty		-11.7	-11.9	-9.4	-11.7	-7.1	-11.3
			MBTA	16	$-10.3^{-3.2}$	$-11.2^{-1.5}$	$-9.2^{-2.7}$	$-10.3^{-2.8}$	$-8.1^{-2.2}$	$-9.0^{-3.7}$
4.0	2.0	0.70	equation of state	46	$-10.3^{-2.7}$	$-11.2^{-1.2}$	$-9.2^{-2.1}_{+0.4}$	$-10.3^{-2.5}$	$-8.1^{-1.5}_{+1.8}$	$-9.0^{-3.3}$
			m_{ej}, v_{ej}		$-11.8^{-1.2}_{+1.1}$	$-12.0^{-0.9}_{+0.8}$	$-9.9^{-1.7}_{+1.9}$	$-11.4^{-0.8}_{+0.3}$	$-8.0^{-2.4}_{+3.0}$	$-10.9^{-0.3}_{+0.2}$
			X_{lan}		$-12.3^{-0.5}_{+4.9}$	$-11.3^{-2.4}_{+0.6}$	$-11.1^{-1.1}_{+5.1}$	$-10.2^{-3.5}_{+2.2}$	$-10.0^{-1.7}_{+6.0}$	$-9.4^{-3.7}_{+4.8}$
			all	14	$-10.4^{-1.7}_{+0.1}$	$-11.2^{-1.9}$	$-9.3^{-1.7}_{+0.1}$	$-10.3^{-2.9}_{+0.1}$	$-8.2^{-2.0}_{+0.1}$	$-8.9^{-3.5}_{+0.1}$

with fixed parameters $m_{\text{chirp}}^{\text{fixed}}$, q^{fixed}, $\chi_{\text{eff}}^{\text{fixed}}$. Moreover, we assume a fixed neutron-star equation of state, EOS$^{\text{fixed}}$. If in addition we assume that the ejecta fits have no errors and we fix the lanthanide fraction to $X_{\text{lan}}^{\text{fixed}}$, then the *Model I* light curves have no uncertainty. From Table 2, one can see that the low-latency pipelines constrain the chirp mass well (around 1 per cent error), while the measured mass ratio and the effective spin have large errors, sometimes over 100 per cent. Therefore, in order to assess the effect of inaccurate measurements in the low-latency pipelines, we consider uniform grid points $(m_{\text{chirp}}, q, \chi_{\text{eff}}) \in [0.99 m_{\text{chirp}}^{\text{fixed}}, 1.01 m_{\text{chirp}}^{\text{fixed}}] \times [\frac{1}{2} q^{\text{fixed}}, \min(2 q^{\text{fixed}}, 1)] \times [-\chi_{\text{eff}}^{\text{fixed}}, \min(3 \chi_{\text{eff}}^{\text{fixed}}, 1)]$. In all our examples $\chi_{\text{eff}}^{\text{fixed}} \geq 0$. On the other hand, the equation of state EOS$^{\text{fixed}}$ and $X_{\text{lan}}^{\text{fixed}}$ are unchanged and we always assume that the ejecta fits have no errors. Similarly, the impact of equation-of-state marginalization on the light-curve output is derived by considering

the entire set of 2396 equations of state and keeping all other parameters set to their initial fixed values. Figs 1 and 2 show that, by using different ejecta fits, one may obtain noticeably different values for the merger expelled matter. The effects of the mass and velocity ejecta fits are probed by considering uniform grid points $(m_{\text{ej}}, v_{\text{ej}}) \in [\frac{1}{3} m_{\text{ej}}^{\text{fixed}}, 3 m_{\text{ej}}^{\text{fixed}}] \times [\frac{1}{2} v_{\text{ej}}^{\text{fixed}}, 2 v_{\text{ej}}^{\text{fixed}}]$ and keeping the lanthanide fraction equal to $X_{\text{lan}}^{\text{fixed}}$. In the preceding expression, $m_{\text{ej}}^{\text{fixed}}$, $v_{\text{ej}}^{\text{fixed}}$ are the mass and velocity of ejecta obtained from $m_{\text{chirp}}^{\text{fixed}}$, q^{fixed}, and $\chi_{\text{eff}}^{\text{fixed}}$. Equally, our limited knowledge about the composition of the ejecta is evaluated by considering one-dimensional uniform grid points $\log_{10} X_{\text{lan}} \in [-9, -1]$, at fixed $m_{\text{ej}} = m_{\text{ej}}^{\text{fixed}}$ and $v_{\text{ej}} = v_{\text{ej}}^{\text{fixed}}$. Finally, we also treat the case of all uncertainty sources combined: we start with $(m_{\text{chirp}}, q, \chi_{\text{eff}}) \in [0.99 m_{\text{chirp}}^{\text{fixed}}, 1.01 m_{\text{chirp}}^{\text{fixed}}] \times [\frac{1}{2} q^{\text{fixed}}, \min(2 q^{\text{fixed}}, 1)] \times [-\chi_{\text{eff}}^{\text{fixed}}, \min(3 \chi_{\text{eff}}^{\text{fixed}}, 1)]$; then we

marginalize over the entire set of 2396 equations of state; for each sample $(m_{\mathrm{ej}}^{\mathrm{predicted}}, v_{\mathrm{ej}}^{\mathrm{predicted}})$ of predicted mass and velocity ejecta, we consider a distribution of samples in $[\frac{1}{3} m_{\mathrm{ej}}^{\mathrm{predicted}}, 3 m_{\mathrm{ej}}^{\mathrm{predicted}}] \times [\frac{1}{2} v_{\mathrm{ej}}^{\mathrm{predicted}}, 2 v_{\mathrm{ej}}^{\mathrm{predicted}}]$; finally, we marginalize with $\log_{10}(X_{\mathrm{lan}})$ uniformly sampled in $[-9, -1]$.

Table 3 summarizes these results for five binaries. The parameters have been chosen in such a way that, based on our knowledge to date, the binaries are as follows: a BNS ($m_1^{\mathrm{fixed}} = 1.6\,\mathrm{M_\odot}$, $m_2^{\mathrm{fixed}} = 1.4\,\mathrm{M_\odot}$, $\chi_{\mathrm{eff}}^{\mathrm{fixed}} = 0.01$); a system that, depending on the neutron-star equation of state, is either a BNS or a NSBH ($m_1^{\mathrm{fixed}} = 2.0\,\mathrm{M_\odot}$, $m_2^{\mathrm{fixed}} = 1.4\,\mathrm{M_\odot}$, $\chi_{\mathrm{eff}}^{\mathrm{fixed}} = 0.01$); a low-spin NSBH ($m_1^{\mathrm{fixed}} = 4.0\,\mathrm{M_\odot}$, $m_2^{\mathrm{fixed}} = 1.4\,\mathrm{M_\odot}$, $\chi_{\mathrm{eff}}^{\mathrm{fixed}} = 0.1$); a high-spin NSBH ($m_1^{\mathrm{fixed}} = 4.0\,\mathrm{M_\odot}$, $m_2^{\mathrm{fixed}} = 1.4\,\mathrm{M_\odot}$, $\chi_{\mathrm{eff}}^{\mathrm{fixed}} = 0.7$); a system that, depending on the supranuclear matter equation of state, is either a NSBH or a BBH and has high spin ($m_1^{\mathrm{fixed}} = 4.0\,\mathrm{M_\odot}$, $m_2^{\mathrm{fixed}} = 2.0\,\mathrm{M_\odot}$, $\chi_{\mathrm{eff}}^{\mathrm{fixed}} = 0.7$). First of all, we remark on the expected behaviour of light-curve uncertainties increasing with time. The most important source of uncertainty turns to be our ignorance about the chemical composition of the ejecta. Letting X_{lan} vary within $[10^{-9}, 10^{-1}]$ is responsible for a difference of up to five magnitudes at the end of the first day. Then the second main source of uncertainty seems to be inaccurate GW strain measurement by low-latency pipelines. The errors are greater when the system is not undoubtedly a BNS. There are at least two simple explanations for this feature: the high uncertainty in the mass ratio implies we are considering systems of different types (BNS and NSBH; NSBH and BBH); in the case of high effective spin $\chi_{\mathrm{eff}}^{\mathrm{fixed}}$, our choice of the variation interval $[-\chi_{\mathrm{eff}}^{\mathrm{fixed}}, \min(3\chi_{\mathrm{eff}}^{\mathrm{fixed}}, 1)]$ has a non-negligible impact on the mass ejecta, as we show in Fig. 2. The last two sources of uncertainty are equation-of-state marginalization and ejecta fit errors. As expected, the effects of equation-of-state marginalization are more substantial when one of the binary components has a mass of about $2\,\mathrm{M_\odot}$. In such a case, by varying the equation of state, we change the type of the compact object. Therefore, low-latency measurement errors have a big influence on *HasEjecta*, especially when the system is high-spinning and has a non-negligible probability of being a NSBH. Similarly, the effect of equation-of-state marginalization on *HasEjecta* is important, as previously highlighted in Fig. 1. It is worth noting that, when all the error sources are considered, the corresponding uncertainty is not the simple sum of the independent errors, since we allow for compensation effects.

In Fig. 5, we show an example of a BNS light-curve contour, illustrating the time evolution of the absolute magnitude in the *r* photometric band corresponding to the different sources of uncertainty. Except for the case of only equation-of-state marginalization uncertainty, in all other cases the true value of the absolute magnitude is included inside the 1σ error. Fig. 5 illustrates again that the main limitations of our pipeline are lack of knowledge regarding the ejecta composition and the imprecise constraint of binary component parameters. In contrast, the *r*-filter 3σ error bar, corresponding to the eventual imprecise ejecta fits, spreads over less than 2 magnitudes after 3 days succeeding compact object coalescence.

5 DEMONSTRATION ON REAL EXAMPLES

In this section, we demonstrate the output of our tool on the following O2/O3a LIGO–Virgo GW events: GW170817 (Abbott et al. 2017b), GW190425 (Abbott et al. 2020c), and GW190814 (Abbott et al. 2020d). GW170817 and GW190425 are BNSs, while GW190814 is either a NSBH or a BBH (cf. the discussion in e.g. Abbott et al. 2020d; Essick & Landry 2020; Most et al. 2020; Tan, Noronha-Hostler & Yunes 2020; Tews et al. 2020). It is worth mentioning that more than
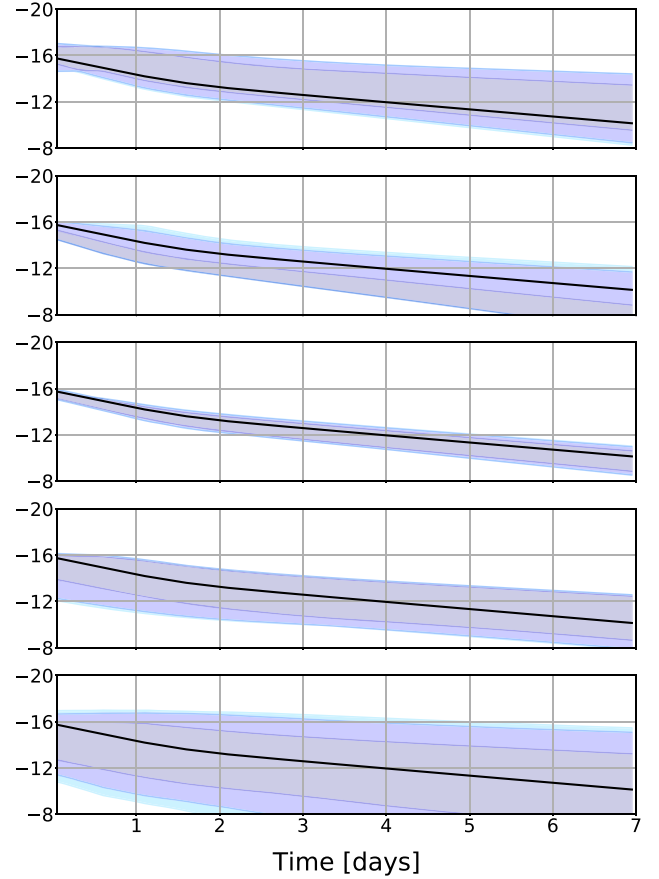

Figure 5. Absolute magnitude versus time for a BNS system with $(m_1^{\mathrm{fixed}}, m_2^{\mathrm{fixed}}, \chi_{\mathrm{eff}}^{\mathrm{fixed}}) = (1.6\,\mathrm{M_\odot}, 1.4\,\mathrm{M_\odot}, 0.01)$. The blue filled bands represent the predicted light curves, assigned with errors. The sources of uncertainty are, from the top panel to the bottom panel, the MBTA low-latency pipeline, the equation-of-state marginalization, the mass and velocity of the ejecta, the lanthanide fraction, and all the uncertainty sources combined. In all panels, the black curve represents the same predicted light curve when there is no uncertainty at all. In this case, the equation of state is EOS$^{\mathrm{fixed}}$, parameterized by $\{\gamma\} = (1.4777, -0.3225, 0.0694, -0.0046)$, and the lanthanide fraction is fixed to $X_{\mathrm{lan}}^{\mathrm{fixed}} = 10^{-4}$. In the contour plots, 1σ, 2σ, and 3σ are indicated in shades of blue, from darkest to lightest. For these simulations we used *Model I*.

98 per cent of the time needed for the code to run is used in the equation-of-state marginalization (presented in Section 3) and light-curve generation (presented in Section 4) processes. More precisely, with a single *E5-2698 v4* processor, we need on average 6.204 s for the equation-of-state marginalization and 0.198 s (respectively 0.471 s) for the computation of a *Model I* (respectively *Model II*) light curve, if only one core is used. In this case, the total necessary time to convert the input low-latency data into kilonova light curves is around $198\,\mathrm{s} + 6.204\,\mathrm{s} \times n_{\mathrm{templates}}$ (respectively $471\,\mathrm{s} + 6.204\,\mathrm{s} \times n_{\mathrm{templates}}$) when *Model I* (respectively *Model II*) is used. In the preceding expression, $n_{\mathrm{templates}}$ is the number of input MBTA templates, which typically is $O(10)$. We note, though, that this computation is easily parallelizable and latency could be reduced. For example, when the same processor is used with eight cores, the times required for the equation-of-state marginalization and *Model I* and *Model II* light-curve computations become 0.975, 0.059, and 0.249 s, which means that the overall code is executed in around $59\,\mathrm{s} + 0.975\,\mathrm{s} \times n_{\mathrm{templates}}$

Table 4. Values of *HasRemnant* (second column) and *HasEjecta*, based on both MBTA (third column) and PE (fourth column) samples, for the O2/O3a compact binary coalescence events: GW170817, GW190425, and GW190814. The values of *HasRemnant* for GW190425 and GW190814 triggers are taken from LIGO Scientific Collaboration & Virgo Collaboration (2019a) and LIGO Scientific Collaboration & Virgo Collaboration (2019b). Given the fact that *HasRemnant* has been introduced at the beginning of 03, for the GW170817 *HasRemnant* we had to assume the same value as for *EM-Bright* reported in Abbott et al. (2019). Regarding the PE results, the samples used for GW170817 (respectively GW190425 and GW190814) are the ones introduced in Abbott et al. (2019) (respectively in Abbott et al. 2020b).

Event	*HasRemnant*	MBTA *HasEjecta*	PE *HasEjecta*
GW170817	100%	100%	100%
GW190425	> 99%	98%	>99%
GW190814	< 1%	0%	0%
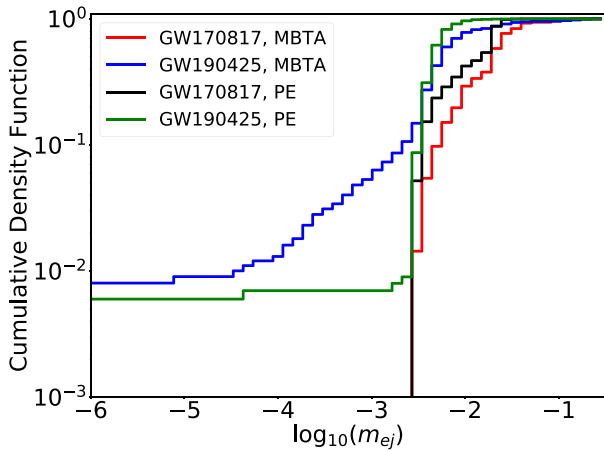
Figure 6. Cumulative distribution function of the ejected mass m_{ej} for the following GW triggers: GW170817, GW190425. Both the low-latency results (the input data are represented by the MBTA weighted templates) and the PE results (the input data are represented by the offline PE (Veitch et al. 2015) posteriors) are shown.

(respectively $249\,\text{s} + 0.975\,\text{s} \times n_{\text{templates}}$) if *Model I* (respectively *Model II*) is employed.

5.1 Comparison of ejecta mass and *HasEjecta*

The definition of *HasEjecta* is similar to that of *HasRemnant* (Chatterjee et al. 2020), a low-latency data-based product provided by the LVC. In Table 4, we compare *HasRemnant* and *HasEjecta* calculated in two ways: (i) the MBTA samples described in Section 2, and (ii) sampling the waveform model posteriors of PE results. From this table, the three quantities give consistent results. From the list of three events mentioned at the beginning of this section, only two of them (GW170817 and GW190425) have non-negligible *HasEjecta*. Therefore in Fig. 6 there is an illustration of the mass ejecta m_{ej} distribution for GW170817 and GW190425. This figure suggests that the low-latency based method presented in this work reproduces fairly well the predictions one could get by means of the offline PE posteriors; however, further studies of other events are required for a final conclusion.

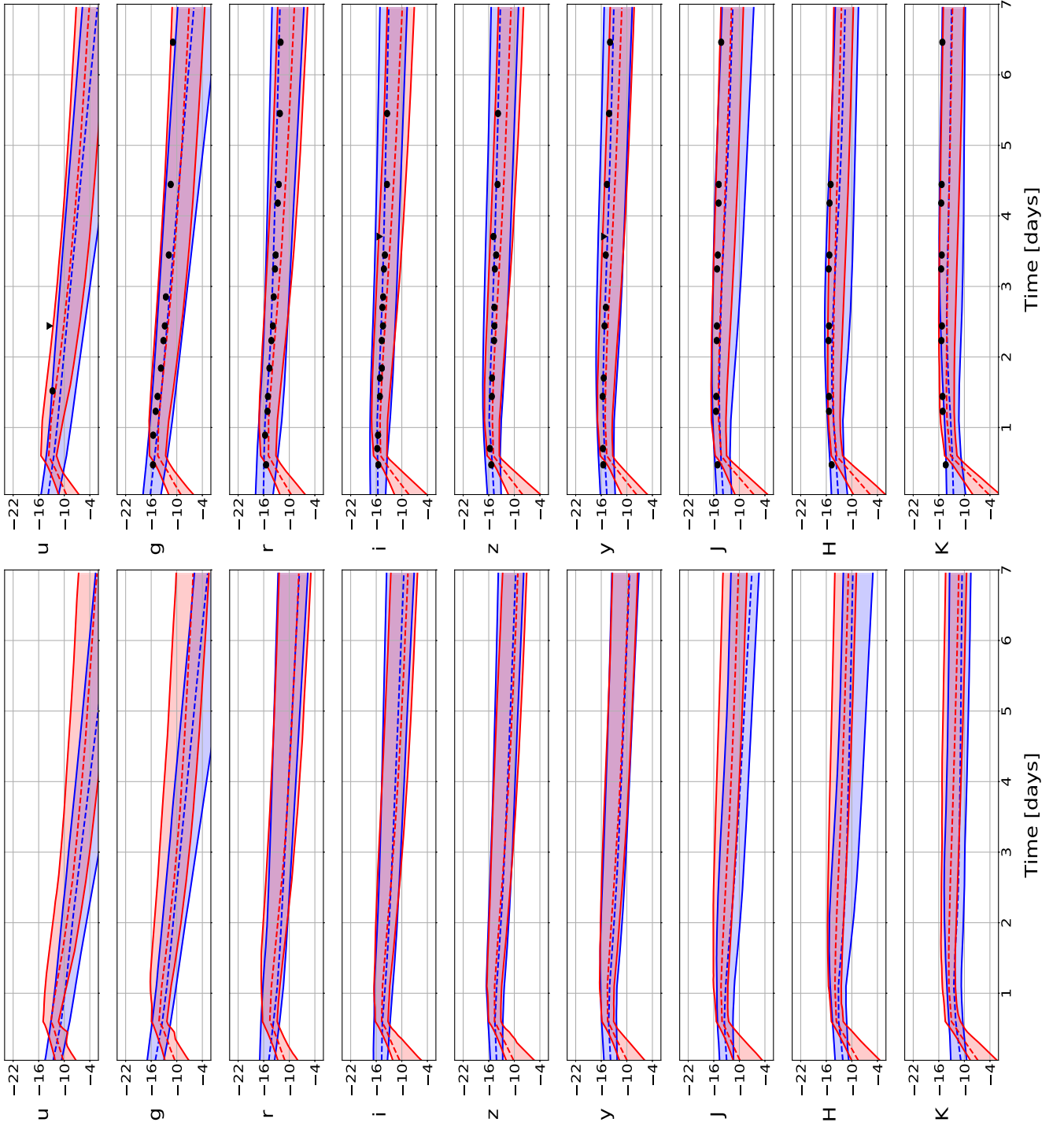### 5.2 Light-curve predictions

In Fig. 7, we illustrate the corresponding light curves employing both *Model I* and *Model II*. Regarding *Model I*, we set the lanthanide fraction for this analysis to $X_{\text{lan}} = 10^{-4}$ (consistent with the results presented in Coughlin et al. 2018b), while, concerning *Model II*, we use a uniform prior in $\cos\theta_{\text{inc}}$ for the inclination angle θ_{inc}, and we fix $\Phi = 45°$ (consistent with the results presented in Dietrich et al. 2020). A significant difference between the two models, clearly highlighted by Fig. 7, concerns the first half-day following the kilonova. *Model I* light curves present a small (negative for the lower wavelengths and positive for the higher wavelengths) slope, while *Model II* has a more pronounced rising shape.

One can observe good agreement between the real data and our predictions in the case of GW170817. Almost all the observational points are included in between the upper and lower limits in the case of *Model I*, whereas the predictions from *Model II* are missing a few more points in the first half day. Nevertheless, the agreement could be strengthened by choosing other parameters (X_{lan}, θ_{inc}, Φ) that are not constrained by the GW data and/or our understanding of compact objects. Also, this suggests that the uncertainty presented here could be significantly underestimated because we fixed these parameters. The *Model I* predictions for GW190425 show that it is less bright than GW170817. Indeed, predictions for GW190425 are at least 1 magnitude higher (i.e. dimmer) in almost all photometric bands after only 1 hour, and at least 3 magnitudes higher after 3 days. This fact, corroborated with the broad skymap localization (LIGO Scientific Collaboration & Virgo Collaboration 2019a), could explain the non-detection of an EM counterpart for GW190425.

In order to convert absolute magnitude into apparent magnitude, we use the distance in the form of the distance modulus: $m - M = 5 \log_{10} d_L - 5$, where m, M, d_L are the apparent magnitude, the absolute magnitude, and the luminosity distance expressed in units of pc. Here, we will use LIGO–Virgo–Kagra based low-latency products, which contain the required distance information. One of the data products released at low latency is the Bayestar skymap (Singer & Price 2016); this skymap provides an array of sky coordinates, each of them assigned with a localization probability, a luminosity distance, and a distance uncertainty. From this skymap a mean distance is calculated. It is worth mentioning that the luminosity distance uncertainty is not taken into account for the calculation of the light-curve contours. For example, the Bayestar distance relative error for GW170817, GW190425, and GW190814 is less than 0.3, which translates to an uncertainty in the apparent magnitude of less than 0.7 mag. Nonetheless, this value is not negligible, as it represents ~20 per cent of the total error budget. This suggests that the uncertainty stated here is underestimated. In Fig. 8 there is an example of contours representing the evolution of the apparent magnitude with time. This figure shows again that the lack of information concerning the chemical composition of the ejecta is responsible for a large uncertainty. Also, this figure emphasizes that, whatever the lanthanide fraction $X_{\text{lan}} \in [10^{-9}, 10^{-1}]$, the output for GW190425 predicts a kilonova with apparent magnitude higher than 21.2 (respectively 20.2) in the g (respectively r) photometric band after only one day, which is in agreement with the ZTF observational data based upper limits presented in Coughlin et al. (2019b).

6 CONCLUSION

In this work, we present a tool aimed at predicting kilonova light curves based on low-latency data products. We propose a way to take advantage of the multiple templates around the preferred

Figure 7. Kilonova light curves (absolute magnitude versus time) predicted by *Model I* (in blue) and *Model II* (in red) for *u, g, r, i, z, y, J, H, K* photometric bands. The predicted light curves for GW170817 (top) and for GW190425 (bottom). For each filter there are three curves plotted: the upper solid line, middle dashed line, and lower solid line represent the 90th, 50th, and 10th percentiles, respectively. In the case of GW170817, the circle and triangle symbols in black illustrate the measured optical points of AT2017gfo. The circle symbols are measured points with finite uncertainty, while triangle symbols are upper limits. The prior $X_{\text{lan}} = 10^{-4}$ (respectively $\Phi = 45°$ and $\cos\theta_{\text{inc}}$ uniform in [0,1]) is used for *Model I* (respectively *Model II*).

event found by low-latency pipelines and show how to predict mass ejecta from preliminary estimates of the binary parameters. We demonstrate the procedure on GW candidates, computing the ejecta probability (*HasEjecta*) reported by our tool and comparing it with the value of *HasRemnant* currently released by the LIGO–

Virgo–Kagra collaborations. We then propose two ways to convert mass ejecta and other parameters such as ejecta velocity, lanthanide fraction, binary inclination angle, and half-opening angle of the lanthanide-rich ejecta component into kilonova light curves. The different sources of error are evaluated. It turns out that the knowledge
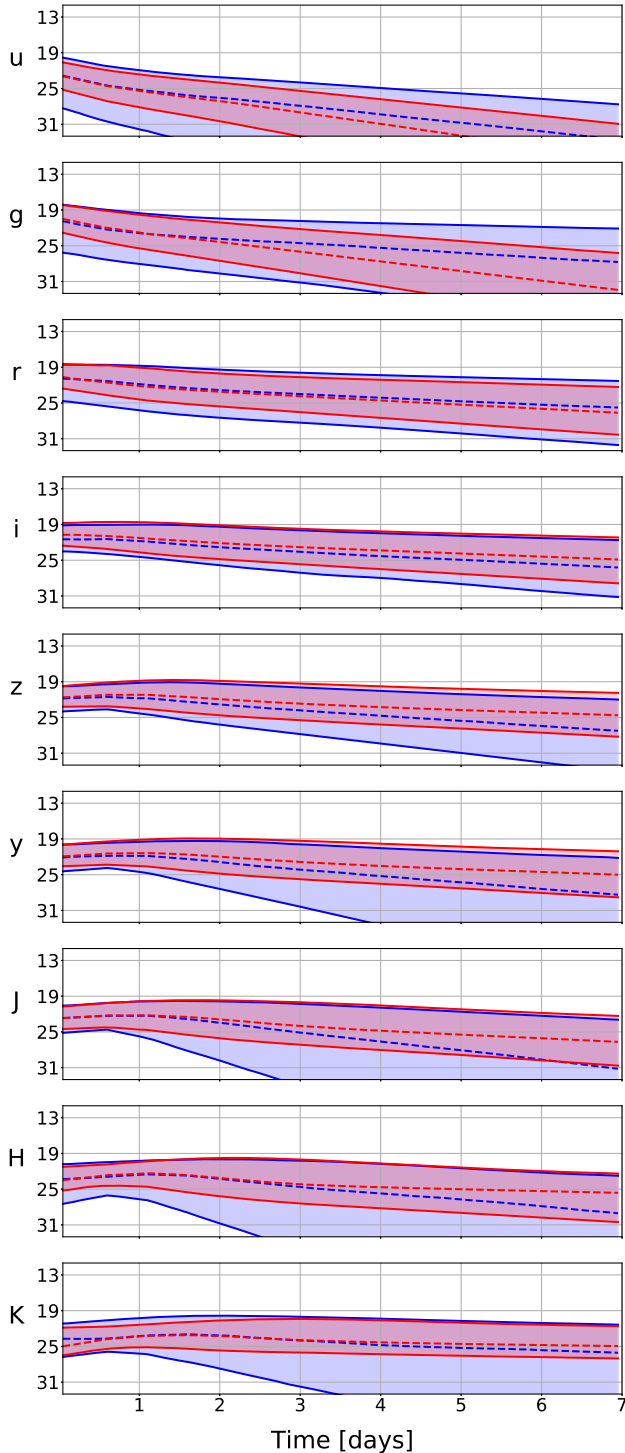
Figure 8. Apparent magnitude versus time based on the offline PE posteriors and LALInference (Veitch et al. 2015) skymap. The presented event is GW190425 and the light curves in blue (respectively red) are predicted by *Model I* with prior $\log_{10}X_{\text{lan}}$ uniform in $[-9, -1]$ (respectively $X_{\text{lan}} = 10^{-4}$).

uncertainty we have regarding the chemical composition of the ejecta is the principal limitation of the method, while the mass-ejecta fit errors have the smallest impact on the light-curve output. We compare our predicted light curve with the only kilonova counterpart observed to date, i.e. AT2017gfo, showing consistency with those results. Finally, we suggest how to convert absolute magnitude to apparent

magnitude by means of the Bayestar skymap. This method can be used during the next observing run O4 as a utility to inform the EM community better concerning the characteristics of the kilonova signal they are trying to catch.

Improvements to the tool can be envisaged. A better treatment of the input low-latency data of LIGO–Virgo–Kagra could be considered: in particular, the availability of low-latency parameter estimation results might be of importance, since the uncertainties in the individual masses are non-negligible and only the chirp mass is quite well measured. On the other hand, the mass ratio for the existing binary population in the Universe has improved considerably during the last years. As a consequence, one way to reduce errors could be to consider only the chirp mass from templates (Margalit & Metzger 2019), but use the mass ratio based on the observed binary population (e.g. Mandel 2010; Abbott et al. 2020a; Essick & Landry 2020; Fishbach et al. 2020a,b). Equally, one could provide light-curve estimates conditioned on the direction to the source, which will probably be what an EM observer would want. Such a development should be easily implementable, given the format of the actual Bayestar and LALInference skymaps. Likewise, more counterparts to binary compact mergers in the next years will improve our understanding of the equation of state of supranuclear dense matter and potentially the ejecta composition and geometry of the different ejecta components. Thereafter, priors like the lanthanide fraction and/or the half-opening angle of some ejecta component, needed for the computation of the light curve made by surrogates, could be addressed more accurately.

DATA AVAILABILITY

The data underlying this article are derived from public code found here: https://github.com/mcoughlin/gwemlight curves. The simulations resulting will be shared on reasonable request to the corresponding author.

REFERENCES

Abbott B. P. et al., 2017a, Phys. Rev. Lett., 119, 161101
Abbott B. P. et al., 2017b, Phys. Rev. Lett., 119, 161101
Abbott B. P. et al., 2017c, ApJ, 848, L12

Abbott B. P. et al., 2017d, ApJ, 848, L13
Abbott B. P. et al., 2018a, Phys. Rev. Lett., 121, 161101
Abbott B. et al., 2018b, Living Reviews in Relativity, 21, 3
Abbott B. P. et al., 2019, Phys. Rev. X, 9, 031040
Abbott B. P. et al., 2019, ApJ, 875, 161
Abbott R. et al., 2020a, Astrophys. J. Lett., 913, L7
Abbott R. et al., 2020b, preprint (arXiv:2010.14527)
Abbott B. et al., 2020c, ApJ, 892, L3
Abbott R. et al., 2020d, ApJ, 896, L44
Alford M. G., Han S., Prakash M., 2013, Phys. Rev. D, 88, 083013
Antier S. et al., 2020a, MNRAS, 492, 3904
Antier S. et al., 2020b, MNRAS, 497, 5518
Aubin F. et al., 2020, Class. Quant. Grav., 38, 095004
Bauswein A., Baumgarte T. W., Janka H.-T., 2013a, Phys. Rev. Lett., 111, 131101
Bauswein A., Baumgarte T., Janka H. T., 2013b, Phys. Rev. Lett., 111, 131101
Bauswein A. et al., 2017, ApJ, 850, L34
Bauswein A., Blacker S., Lioutas G., Soultanis T., Vijayan V., Stergioulas N., 2020, Phys. Rev. D, 103, 123004
Bellm E. C. et al., 2018, PASP, 131, 018002
Berry C. P. L. et al., 2015, ApJ, 804, 114
Biscoveanu S., Vitale S., Haster C.-J., 2019, ApJ, 884, L32
Bloemen S., Groot P., Nelemans G., Klein-Wolt M., 2015, in Rucinski S. M., Torres G., Zejda M., eds, ASP Conf. Ser. Vol. 496, Living Together: Planets, Host Stars and Binaries. Astron. Soc. Pac., San Francisco, p. 254
Bogdanov S. et al., 2019, ApJ, 887, L25
Bovard L., Martin D., Guercilena F., Arcones A., Rezzolla L., Korobkin O., 2017, Phys. Rev. D, 96, 124005
Breschi M., Perego A., Bernuzzi S., Del Pozzo W., Nedora V., Radice D., Vescovi D., 2021, MNRAS, 505, 1661
Breu C., Rezzolla L., 2016, MNRAS, 459, 646
Bulla M., 2019, MNRAS, 489, 5037 (Model II)
Cannon K. et al., 2020, SoftwareX, 14, 100680
Capano C. D. et al., 2020, Nature Astron., 4, 625
Chatterjee D., Ghosh S., Brady P. R., Kapadia S. J., Miller A. L., Nissanke S., Pannarale F., 2020, ApJ, 896, 54
Chatziioannou K., Han S., 2020, Phys. Rev. D, 101, 044019
Chen H.-Y., Essick R., Vitale S., Holz D. E., Katsavounidis E., 2017, ApJ, 835, 31
Christie I. M., Lalakos A., Tchekhovskoy A., Fernández R., Foucart F., Quataert E., Kasen D., 2019, MNRAS, 490, 4811
Cornish N. J., Littenberg T. B., 2015, Classical and Quantum Gravity, 32, 135012
Cornish N. J., Littenberg T. B., Bécsy B., Chatziioannou K., Clark J. A., Ghonge S., Millhouse M., 2021, Phys. Rev. D, 103, 044006
Coughlin M. W., Dietrich T., 2019, Phys. Rev. D, 100, 043011
Coughlin M., Dietrich T., Kawaguchi K., Smartt S., Stubbs C., Ujevic M., 2017, ApJ, 849, 12
Coughlin M. W. et al., 2018a, MNRAS, 480, 3871
Coughlin M. W. et al., 2018b, MNRAS, 480, 3871
Coughlin M. W., Dietrich T., Margalit B., Metzger B. D., 2019a, MNRAS, 489, L91
Coughlin M. W. et al., 2019b, ApJ, 885, L19
Coughlin M. W. et al., 2020a, Nature Communications, 11, 4129
Coughlin M. W. et al., 2020b, MNRAS, 492, 863
Coughlin M. W. et al., 2020c, MNRAS, 497, 1181
Coulter D. A. et al., 2017, Science, 358, 1556
Dal Canton T., Nitz A. H., Gadre B., Davies G. S., Villa-Ortega V., Dent T., Harry I., Xiao L., 2020, preprint (arXiv:2008.07494)
Dal Canton T. et al., 2014, Phys. Rev. D, 90, 082004
Dekany R. et al., 2020, PASP, 132, 038001
Dietrich T., Ujevic M., 2017, Classical and Quantum Gravity, 34, 105014
Dietrich T. et al., 2018, Class. Quant. Grav., 35, 24LT01
Dietrich T., Coughlin M. W., Pang P. T. H., Bulla M., Heinzel J., Issa L., Tews I., Antier S., 2020, Science, 370, 1450
Douchin F., Haensel P., 2001, A&A, 380, 151
Essick R., Landry P., 2020, ApJ, 904, 80

Essick R., Vitale S., Katsavounidis E., Vedovato G., Klimenko S., 2015, ApJ, 800, 81
Essick R., Landry P., Holz D. E., 2020a, Phys. Rev. D, 101, 063007
Essick R., Tews I., Landry P., Reddy S., Holz D. E., 2020b, Phys. Rev. C, 102, 055803
Fairhurst S., 2009, New J. Phys., 11, 123006
Fairhurst S., 2011, Classical and Quantum Gravity, 28, 105021
Fernández R., Kasen D., Metzger B. D., Quataert E., 2015, MNRAS, 446, 750
Fernández R., Tchekhovskoy A., Quataert E., Foucart F., Kasen D., 2019, MNRAS, 482, 3373
Fishbach M., Farr W. M., Holz D. E., 2020a, ApJ, 891, L31
Fishbach M., Essick R., Holz D. E., 2020b, ApJ, 899, L8
Foucart F., 2012, Phys. Rev. D, 86, 124007
Foucart F., 2020, Front. Astron. Space Sci., 7, 46
Foucart F., Hinderer T., Nissanke S., 2018, Phys. Rev. D, 98, 081501
Foucart F., Duez M., Kidder L., Nissanke S., Pfeiffer H., Scheel M., 2019, Phys. Rev. D, 99, 103025
Goldstein A. et al., 2017, ApJ, 848, L14
Gompertz B. P. et al., 2020, MNRAS, 497, 726
Goriely S., Bauswein A., Janka H.-T., 2011, ApJ, 738, L32
Graham M. J. et al., 2019, PASP, 131, 078001
Grossman D., Korobkin O., Rosswog S., Piran T., 2014, MNRAS, 439, 757
Grover K., Fairhurst S., Farr B. F., Mandel I., Rodriguez C., Sidery T., Vecchio A., 2014, Phys. Rev. D, 89, 042004
Han S., Mamun M., Lalit S., Constantinou C., Prakash M., 2019, Phys. Rev. D, 100, 103022
Heinzel J. et al., 2021, MNRAS, 502, 3057
Hinderer T. et al., 2019, Phys. Rev. D, 100, 06321
Hooper S., Chung S. K., Luan J., Blair D., Chen Y., Wen L., 2012, Phys. Rev. D, 86, 024012
Ivezic Z., Tyson J. A., Allsman R., Andrew J., Angel R., 2019, ApJ, 873, 111
Kapadia S. J. et al., 2020, Classical and Quantum Gravity, 37, 045007
Kasen D., Metzger B., Barnes J., Quataert E., Ramirez-Ruiz E., 2017, Nature, 551, 80
Kawaguchi K., Kyutoku K., Shibata M., Tanaka M., 2016, ApJ, 825, 52
Kawaguchi K., Shibata M., Tanaka M., 2020, ApJ, 889, 171
Klimenko S., Yakushin I., Mercer A., Mitselmakher G., 2008, Classical and Quantum Gravity, 25, 114029
Klimenko S. et al., 2016, Phys. Rev. D, 93, 042004
Krüger C. J., Foucart F., 2020, Phys. Rev. D, 101, 103002
Krüger C. J., Foucart F., 2020, Phys. Rev. D, 101, 103002
Landry P., Essick R., 2019, Phys. Rev. D, 99, 084049
Landry P., Essick R., Chatziioannou K., 2020, Phys. Rev. D, 101, 123007
Lange J., O'Shaughnessy R., Rizzo M., 2018, preprint (arXiv:1805.10457)
Lattimer J. M., Prakash M., 2001, ApJ, 550, 426
Lattimer J. M., Schramm D. N., 1974, ApJ, 192, L145
LIGO Scientific Collaboration, Virgo Collaboration, 2019a, GRB Coordinates Network, 24168, 1
LIGO Scientific Collaboration, Virgo Collaboration, 2019b, GRB Coordinates Network, 25324, 1
Li L.-X., Paczynski B., 1998, ApJ, 507, L59
Lindblom L., 1998, Phys. Rev. D, 58, 024008
Lindblom L., 2010, Phys. Rev. D, 82, 103011
Lindblom L., Indik N. M., 2012, Phys. Rev. D, 86, 084003
Lindblom L., Indik N. M., 2014, Phys. Rev. D, 89, 064003
Lynch R., Vitale S., Essick R., Katsavounidis E., Robinet F., 2017, Phys. Rev. D, 95, 104046
Mandel I., 2010, Phys. Rev. D, 81, 084029
Margalit B., Metzger B. D., 2019, ApJ, 880, L15
Masci F. J. et al., 2018, PASP, 131, 018003
Metzger B. D. et al., 2010, MNRAS, 406, 2650
Miller M. et al., 2019, ApJ, 887, L24
Morgan J. S., Kaiser N., Moreau V., Anderson D., Burgett W., 2012, Proc. SPIE Int. Soc. Opt. Eng., 8444, 0H
Most E. R., Papenfort L. J., Weih L. R., Rezzolla L., 2020, MNRAS, 499, L82
Nedora V. et al., 2020, preprint (arXiv:2011.11110)

Nicholl M., Margalit B., Schmidt P., Smith G. P., Ridley E. J., Nuttall J., 2021, MNRAS, preprint (arXiv:2102.02229)

Pang P. T., Dietrich T., Tews I., Van Den Broeck C., 2020, Phys. Rev. Res., 2, 033514

Pankow C., Brady P., Ochsner E., O'Shaughnessy R., 2015, Phys. Rev. D, 92, 023002

Pannarale F., Ohme F., 2014, ApJ, 791, L7

Perego A., Radice D., Bernuzzi S., 2017, ApJ, 850, L37

Piran T., Nakar E., Rosswog S., 2013, MNRAS, 430, 2121

Raaijmakers G. et al., 2020, ApJ, 893, L21

Raaijmakers G. et al., 2021, preprint (arXiv:2102.11569)

Radice D., Dai L., 2018, Eur. Phys. J. A, 55, 50

Radice D., Perego A., Hotokezaka K., Fromm S. A., Bernuzzi S., Roberts L. F., 2018a, Astrophys. J., 869, 130

Radice D., Perego A., Zappa F., Bernuzzi S., 2018b, ApJ, 852, L29

Riley T. E. et al., 2019, ApJ, 887, L21

Rosswog S., Korobkin O., Arcones A., Thielemann F., Piran T., 2014, MNRAS, 439, 744

Röver C., Meyer R., Guidi G. M., Viceré A., Christensen N., 2007, Classical and Quantum Gravity, 24, S607

Sachdev S. et al., 2019, Phys. Rev. D, preprint (arXiv:1901.08580)

Salafia O. S., Colpi M., Branchesi M., Chassande-Mottin E., Ghirlanda G., Ghisellini G., Vergani S. D., 2017, ApJ, 846, 62

Savchenko V. et al., 2017, ApJ, 848, L15

Schnittman J. D., Dal Canton T., Camp J., Tsang D., Kelly B. J., 2018, ApJ, 853, 123

Shibata M., Taniguchi K., 2011, Living Rev. Rel., 14, 6

Shibata M., Fujibayashi S., Hotokezaka K., Kiuchi K., Kyutoku K., Sekiguchi Y., Tanaka M., 2017, Phys. Rev. D, 96, 123012

Sidery T. et al., 2014, Phys. Rev. D, 89, 084060

Siegel D. M., Metzger B. D., 2018, ApJ, 858, 52

Singer L. P. et al., 2016, ApJ, 829, L15

Singer L. P., Price L. R., 2016, Phys. Rev. D, 93, 024013

Singer L. P. et al., 2014, ApJ, 795, 105

Smartt S. J. et al., 2017, Nature, 551, 75

Smith R. J. E., Ashton G., Vajpeyi A., Talbot C., 2020, MNRAS, 498, 4492

Sridhar N., Zrake J., Metzger B. D., Sironi L., Giannios D., 2021, MNRAS, 501, 3184

Sutton P. J. et al., 2010, New J. Phys., 12, 053034

Tan H., Noronha-Hostler J., Yunes N., 2020, Phys. Rev. Lett., 125, 261104

Tanaka M., Hotokezaka K., 2013, ApJ, 775, 113

Tews I., Pang P. T., Dietrich T., Coughlin M. W., Antier S., Bulla M., Heinzel J., Issa L., 2020, Astrophys. J. Lett., 908, L1

Tonry J. L. et al., 2018, PASP, 130, 064505

Veitch J. et al., 2015, Phys. Rev. D, 91, 042003

Wen L., Chen Y., 2010, Phys. Rev. D, 81, 082001

This paper has been typeset from a TeX/LaTeX file prepared by the author.